

Water Resources Research

RESEARCH ARTICLE

10.1002/2014WR015574

Key Points:

- Beach mixing zone varied over tidal, spring-neap, and seasonal cycles
- Salinity varies most strongly in response to seasonal inland water table changes
- Beach groundwater dynamics have implications for biogeochemical cycling

Supporting Information:

- Readme
- Figure S1

Correspondence to:

H. A. Michael,
hmichael@udel.edu

Citation:

Heiss, J. W., and H. A. Michael (2014),
Saltwater-freshwater mixing dynamics
in a sandy beach aquifer over tidal,
spring-neap, and seasonal cycles,
Water Resour. Res., 50, doi:10.1002/
2014WR015574.

Received 13 MAR 2014

Accepted 22 JUL 2014

Accepted article online 30 JUL 2014

Saltwater-freshwater mixing dynamics in a sandy beach aquifer over tidal, spring-neap, and seasonal cycles

James W. Heiss¹ and Holly A. Michael^{1,2}

¹Department of Geological Sciences, University of Delaware, Newark, Delaware, USA, ²Department of Civil and Environmental Engineering, University of Delaware, Newark, Delaware, USA

Abstract The biogeochemical reactivity of sandy beach aquifers is closely linked to physical flow and solute transport processes. Thus, a clearer understanding of the hydrodynamics in the intertidal zone is needed to accurately estimate chemical fluxes to the marine environment. A field and numerical modeling study was conducted over a 1 year timeframe to investigate the combined effects of tidal stage, spring-neap variability in tidal amplitude, and seasonal inland water table oscillations on intertidal salinity and flow dynamics within a tide-dominated, microtidal sandy beach aquifer. Measured and simulated salinities revealed an intertidal saline circulation cell with a structure and cross-sectional mixing zone area that varied over tidal, spring-neap, and seasonal time scales. The size of the circulation cell and area of the mixing zone were shown for the first time to be most affected by seasonal water table oscillations, followed by tidal amplitude and tidal stage. The intertidal circulation cell expanded horizontally and vertically as the inland water table declined, displacing the fresh discharge zone and lower interface seaward. Over monthly spring-neap cycles, the center of the circulation cell shifted from beneath the backshore and upper beachface to the base of the beach. Salinity variations in the intertidal zone over semidiurnal tidal cycles were minimal. The dynamics of the circulation cell were similar in simulations with and without a berm. The highly transient nature of intertidal salinity over multiple time scales may have important implications for the types and rates of chemical transformations that occur in groundwater prior to discharge to the ocean.

1. Introduction

Surface water discharge to the sea has historically been thought to be the primary source of land-derived nutrients and other contaminants entering nearshore marine ecosystems. More recently, however, submarine groundwater discharge (SGD) has been identified as an important transport pathway [Johannes, 1980; Simmons, 1992; Moore, 1996; Taniguchi *et al.*, 2002; Moore *et al.*, 2008]. SGD is composed of freshwater from terrestrial sources and seawater circulated across the aquifer-ocean interface. A significant proportion of total SGD discharges through intertidal and nearshore zones of beach aquifers [Li *et al.*, 1999; Bokuniewicz *et al.*, 2004; Robinson *et al.*, 2007c], which are biogeochemically active mixing zones [Charette and Sholkovitz, 2002; Beck *et al.*, 2007; Roy *et al.*, 2013].

Groundwater flow and solute transport in coastal aquifers are influenced by multiple forcing mechanisms that operate over a wide range of temporal and spatial scales, leading to a complex and dynamic intertidal subsurface environment. There are four primary forcing mechanisms that affect freshwater-saltwater dynamics in coastal aquifers (Figure 1). Fresh groundwater exits the aquifer through a narrow discharge zone between the shoreline and the intersection of the lower interface and the seabed (Process 1, Figure 1) [Glover, 1959]. The fresh discharge zone is bounded seaward by the lower interface and landward by an intertidal brackish-saline circulation cell [Robinson *et al.*, 1998; Michael *et al.*, 2005]. Saltwater-freshwater mixing along the lower interface creates a density gradient that drives convective saltwater circulation (Process 2, Figure 1) [Cooper, 1959; Kohout, 1960]. In the intertidal zone, tidal and wave action drive seawater into the beach aquifer, forming a saltwater circulation cell above the zone of seaward-flowing freshwater (Processes 3 and 4, Figure 1) [Lebbe, 1999; Boufadel, 2000; Robinson *et al.*, 2006; Bakhtyar *et al.*, 2012]. Resulting hydraulic head gradients cause seawater to circulate downward and seaward, discharging near the base of the beach [e.g., Michael *et al.*, 2005; Robinson *et al.*, 2006]. A saltwater-freshwater mixing zone forms along the perimeter of this intertidal circulation cell [e.g., Ullman *et al.*, 2003; Turner and Acworth, 2004; Vandenbohede and Lebbe, 2005; Xin *et al.*, 2010; Abarca *et al.*, 2013].

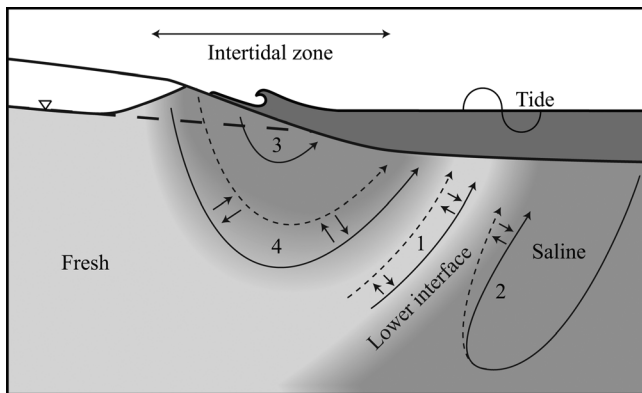


Figure 1. Forcing mechanisms of freshwater flow and saline groundwater recirculation in a coastal aquifer system. Solid and dashed lines represent flow paths. Process 1 is freshwater discharge driven by the inland hydraulic gradient, Process 2 is density-driven circulation along the lower saltwater-freshwater interface, Process 3 is tide-induced circulation. Flow paths marked by a solid and dashed line represent conditions under a weak and strong inland hydraulic gradient, respectively.

intertidal zone [Ullman et al., 2003; Charette and Sholkovitz, 2006]. Thus, a more comprehensive understanding of the dynamics and size of the mixing zone and the variability of discharge caused by both marine and terrestrial driving forces will improve prediction of chemical fluxes to the marine environment through SGD.

The saltwater circulation cell has been observed in a range of field settings under a variety of forcing conditions. The majority of previous field observations provide insight into the geometry and size of the circulation cell at one point in time [Ullman et al., 2003; Turner and Acworth, 2004; Michael et al., 2005; Charette and Sholkovitz, 2006; Robinson et al., 2006; Gibbes et al., 2007]. Other studies reveal that intertidal salinity is sensitive to tidal stage over a tidal cycle [e.g., Henderson et al., 2009; Befus et al., 2013], tidal amplitude [e.g., Robinson et al., 2007a; Abarca et al., 2013], and precipitation [e.g., Santos et al., 2008; Li et al., 2009; Jun et al., 2013]. Spring-neap variability in tidal amplitude has been shown to affect the structure of the circulation cell more than tidal stage [i.e., Robinson et al., 2007a], but the response of the circulation cell to seasonal oscillations in freshwater inflow has not been observed in the field.

The transient nature of the circulation cell when forced with tides has been simulated numerically [Boufadel, 2000; Vandenboheide and Lebbe, 2005; Robinson et al., 2006; Werner and Lockington, 2006; Li et al., 2008; Boufadel et al., 2011; Kuan et al., 2012]. Simulation results indicate that intertidal salinity can vary with tidal stage [Li et al., 2008] and is dependent on the amplitude of a sinusoidal tide [Robinson et al., 2007b]. Changes in tidal amplitude over a spring-neap cycle have also been shown to affect the structure of the circulation cell [Robinson et al., 2007a; Abarca et al., 2013]. Robinson et al. [2007b] and Kuan et al. [2012] showed that the freshwater flux is an important control on the salinity distribution under a semidiurnal tide with a steady head or freshwater flux at the landward boundary. However, transient changes in landward gradient have not been investigated numerically. While the dynamic nature of these systems is becoming clearer, the forcing conditions (i.e., tidal stage, diurnal variability in tidal amplitude, changes in tidal amplitude over a spring-neap cycle, and seasonality in the inland freshwater gradient) have yet to be combined into a continuous numerical model of flow and solute transport to understand how the physical processes interact to affect salinity and flow in the coastal aquifer.

The goal of this study is to identify the physical forcing conditions and time scales that are most important for controlling the structure and areal extent of the intertidal salinity distribution. The forcing conditions that we consider are: (1) tidal stage, (2) spring-neap variability in tidal amplitude, and (3) seasonal fluctuations in the inland water table. The effect of these processes on mixing are examined in the field along a shore-perpendicular transect of multilevel sampling wells. A density-dependent numerical model of groundwater flow and salt transport in a beach aquifer is developed to further explore the dynamics. We also investigate the significance of berm overtopping in modifying the structure and spatial extent of the upper circulation cell. The experimental and simulation results demonstrate the transient response of the intertidal mixing zones and SGD over these time scales.

The mixing of salt water and fresh-water caused by the processes discussed above creates zones of biogeochemical reactivity in the nearshore aquifer [Charette and Sholkovitz, 2002; Kroeger and Charette, 2008; Spiteri et al., 2008; Robinson et al., 2009]. These zones have implications for the fate of land-derived contaminants discharging to coastal surface waters (see review in Slomp and Van Cappellen [2004]), including transformation of nutrients prior to discharge [Bratton et al., 2004; Kroeger and Charette, 2008; Santos et al., 2008; Santoro, 2010; Charbonnier et al., 2013]. The biogeochemical processes are closely tied to the subsurface salinity distribution in the

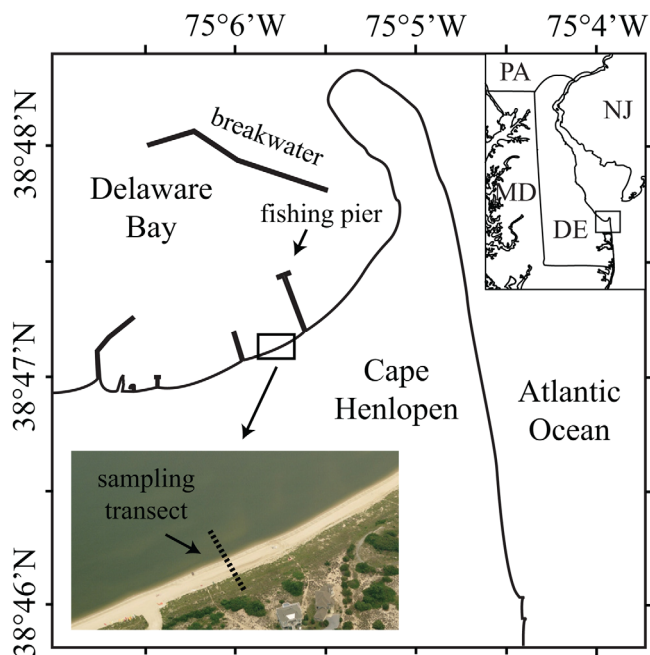


Figure 2. Study area and sampling transect.

2. Study Area Description and Methodology

2.1. Study Area

This study was conducted in the intertidal zone of a microtidal sandy beach that has been the focus of a number of hydrologic and geochemical studies [e.g., *Miller and Ullman, 2004; Hays and Ullman, 2007; Heiss et al., 2014*] (Figure 2). Cape Henlopen is a sandy spit with a regressive sequence; 12–18 m of very coarse sands and gravels overlie marine silts and clays. The morphology of the beach consists of a dune, a 21 m wide backshore, a 14 m wide beachface with a 1:9 slope, and a broad tidal sandflat. A berm crest separates the backshore from the beachface, leading to a low-lying area in the backshore (Figure 3).

The study site is partially protected by offshore breakwaters and therefore experiences little wave action except during storms. Tides are semidiurnal with a range of 1.42 m between MLLW and MHHW (NOAA tidal station 8557830, Lewes, Delaware). Tidal range varies from approximately 2.0 at spring tides to 0.9 m at neap tides. Surface water salinity in the bay is typically ~28 ppt year-round based on monthly surface water measurements, whereas seawater on the ocean side of the spit is 35 ppt.

Hydrogeological characteristics of the study site were determined from sediment samples. Grain size analyses conducted using standard sieving procedures indicate that the beach is composed of predominantly coarse sand with grain sizes ranging from 540 to 668 μm . Measured hydraulic conductivity values from constant head permeameter tests ranged from 27.6 to 30.2 m/d. The hydraulic conductivity of the beach based on the effective grain size and the U.S. Bureau of Reclamation formula [*Vukovic and Soro, 1992*] is 30.2 m/d, consistent with the permeameter measurements.

2.2. Field Measurements

Pore water was sampled for salinity along a shore-perpendicular transect of 10 multilevel samplers. The samplers were constructed from three to five sections of 7 mm OD polyethylene tubing mounted to a

13 mm OD PVC pipe. Each section of tubing was screened over 3 cm and attached to the PVC pipe at depth intervals ranging from 0.5 to 1.0 m. The samplers were installed along the intertidal transect into the beach aquifer, which we consider to extend horizontally from the dune to the base of the beachface, and vertically from the sand surface to the first confining unit (Figure 3).

Pore water was sampled for salinity over a range of time scales. A profile was obtained 9 times over a tidal cycle, on average every 1.6 h on 17 November 2012. Pore water was

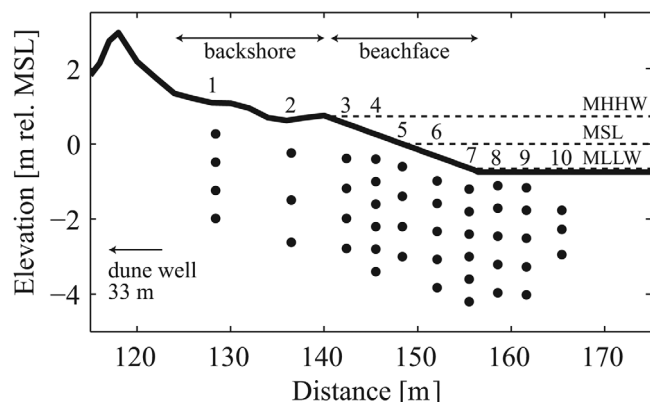


Figure 3. Cross section of sampling transect showing beach morphology and distribution of sampling ports. Distance is meters from landward model boundary.

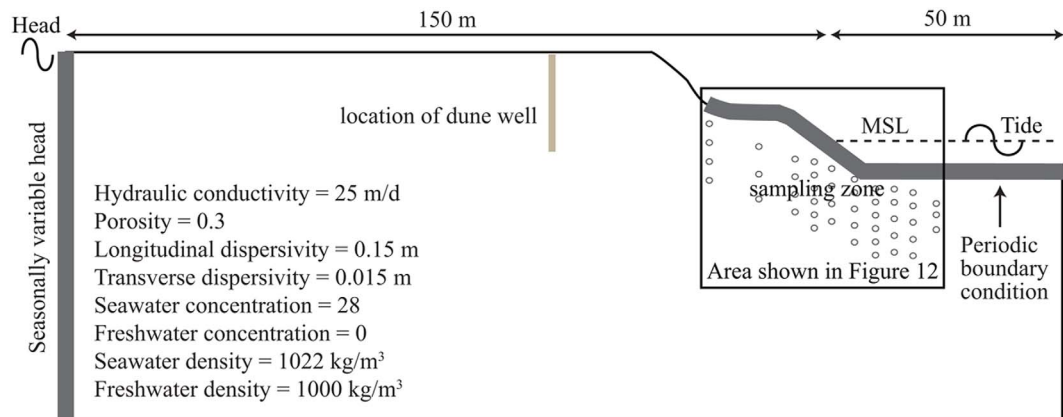


Figure 4. Model domain, boundary conditions, aquifer parameters, and sampling zone. Thin gray lines are no-flow boundaries.

also collected 7 times over a lunar synodic month (29.5 days from new moon to new moon) on average every 4.6 days from 17 November to 14 December 2012 to assess spring-neap variability. Samples were collected 14 times over 1 year from 7 May 2012 to 7 May 2013 on average every 27 days, to examine seasonal variability in salinity. An additional salinity profile was taken on 30 October 2012, 1 day following the landfall of Hurricane Sandy 85 km northeast of the site. Pore water was sampled during the same tidal cycle and phase (at low tide during monthly spring tides) to reduce variability caused by tidal fluctuations and changes in tidal amplitude over spring-neap cycles.

The sampling procedure began with the farthest landward sampler and continued seaward along the transect, ending on the sandflat for a total of 45 pore water samples. Several tube volumes of pore water were pumped from each sample tube using a peristaltic pump before sample collection. A complete profile took no longer than 30 min to complete and is assumed representative of groundwater salinity at one point in time. Salinity was measured as electrical conductivity (YSI EC300) and is reported as ppt.

A conservative tracer solution was injected into the beach at the high tide mark on 28 February 2012 during high tide to determine the residence time and velocity of circulating salt water for model calibration. The 0.18 M KBr tracer solution was designed to have the same 1.022 kg/L density as the bay water (22 g KBr + 1 L deionized H₂O). The injection took place at the shallowest port at multilevel sampler 3 prior to the tide inundating the sand surface above the injection point and continued until high tide, lasting approximately 30 min. Pore water was sampled twice daily from all 45 ports for 7 days for a total of 14 sample times. Bromide concentration was measured with a bromide electrode and the mV output readings were converted to concentration using a calibration curve created from molar standards. The standards were prepared by diluting the 0.18 M solution with bay water and groundwater over a range of expected salinities.

Hydrologic and meteorological data were recorded on each sampling date. The elevation of the water table 33 m behind the dune (herein referred to as the “dune water table”) was recorded at 15 min intervals over the 1 year monitoring period. The water table measurements were used to indicate changes in the inland hydraulic gradient, defined as the gradient between the dune well and the shoreline. Tide elevations at the study site were determined from the nearby Lewes, DE tide gauge station located 1 km east of the transect. Comparison of the NOAA gauge station data with tide levels measured at the transect indicate that there is no time lag or amplitude variation in the tidal signal between the gauge station and the study site. Daily rainfall at the Rehoboth Beach weather station 8 km south of Cape Henlopen was used as a proxy for precipitation at the study site.

2.3. Numerical Model

A variable-density groundwater flow and solute transport model was developed to support the interpretations of instantaneous observations and provide insight into the continuous response of the beach aquifer to tidal variations and seasonally variable inland freshwater forcing. The density-dependent groundwater flow and solute transport code SEAWAT [Langevin *et al.*, 2008] was used to perform the simulations. The coupled flow and solute transport governing equations in SEAWAT are solved using a cell-centered finite

difference approximation. The model represented a 2-D cross section of the unconfined coastal aquifer at Cape Shores. The grid was nonuniform with higher horizontal discretization in the intertidal zone (0.3 m) where higher flow rates and concentration gradients occurred. Sensitivity tests showed that the numerical solution was independent of the grid discretization.

The model domain extended 50 m seaward of the beachface-MSL intersection and 150 m landward (Figure 4). The aquifer extended 15 m below the beach surface to the first silt-clay confining unit [Kraft, 1971]. The beachface and backshore profile used in the model was the average of four profiles that were measured quarterly. The profiles varied by up to 25 cm with the largest differences occurring in the backshore between summer and winter.

2.3.1. Boundary Conditions

The boundary conditions used in the model were chosen to mimic natural forcing conditions. The landward boundary was set as a time-varying head boundary (Dirichlet boundary; Figure 4) using four stress periods to represent seasonal water table fluctuations (Figure 5b). The amplitude of the head fluctuation at the landward boundary was adjusted until the simulated seasonal trend in head at the dune well closely matched the measured seasonal trend in head at that location. The measured and simulated seasonal trends were calculated using locally weighted least squares regression with a first degree polynomial (Figure 5b). The period of the oscillating landward boundary repeated each year; this was consistent with field observations which showed similar heads during May-June 2012 and May-June 2013. The top, bottom, and seaward boundaries were set as no flow (Figure 4). Tidal forcing was simulated along the aquifer-ocean interface using the Periodic Boundary Condition (PBC) package [Post, 2011]. The PBC package was used to allow seepage face development along the aquifer-ocean interface and to apply a multiple-constituent tidal signal to the interface nodes as a time-varying Dirichlet boundary condition. The five tidal constituents with the greatest amplitude at our site according to the NOAA tidal station were used to develop a synthetic tidal signal to match the tide over the 1 year sampling period. The constituents used to generate the signal are the principle lunar semidiurnal (M_2), principle solar semidiurnal (S_2), larger lunar elliptic semidiurnal (N_2), and the lunar diurnal constituents (K_1 and O_1 ; Table 1). The following prediction formula was used:

$$h_t = h_o + \sum_{i=1}^5 A_i \cos(\omega_i t - \theta_i)$$

where h_t (m rel. MSL) is the predicted tidal elevation, h_o (m) is the reference water level (in this case MSL), A_i (m) is the amplitude, ω_i ($\omega_i = \frac{2\pi}{T}$) is the frequency in rad s⁻¹, and θ_i (rad) is the phase of each tidal constituent, i . The measured and predicted tides are shown in Figures 5c and 5d, respectively. The deviation between the predicted and measured tides (average of 15 cm) is due to weather conditions that are not taken into account by the predictions, which are based only on astronomical factors.

The transport boundary condition along the aquifer-ocean interface was zero-concentration gradient for outward flow and a constant concentration of 28 for inward flow. The salinity of inflowing water was thus equal to that of the surface water and the salinity of the discharging groundwater was equal to the concentration of groundwater in the adjacent cell. A constant concentration of 0 was set along the landward vertical boundary and zero mass flux across the no-flow boundaries.

2.3.2. Model Calibration

Model calibration was performed by manually adjusting aquifer parameters, including hydraulic conductivity, porosity, and longitudinal and transverse dispersivity until simulated hydraulic heads and concentrations during the 1 year simulation period and flow velocities during the tracer test matched the field measurements well. The aquifer parameters used in the model are shown in Figure 4. The calibrated hydraulic conductivity of 25 m/d is close to the range of measured hydraulic conductivity (27.6–30.2 m/d).

3. Results and Discussion

3.1. Field Observations

3.1.1. Dune Water Table

Hydraulic head at the dune responded to changes in tidal stage, tidal amplitude, precipitation events, and seasonal variability in recharge (Figures 5a and 5b). Over a tidal cycle, the dune water table typically fluctuated between 5 and 10 cm depending on the amplitude of the tide. The water table fluctuated 10–25 cm

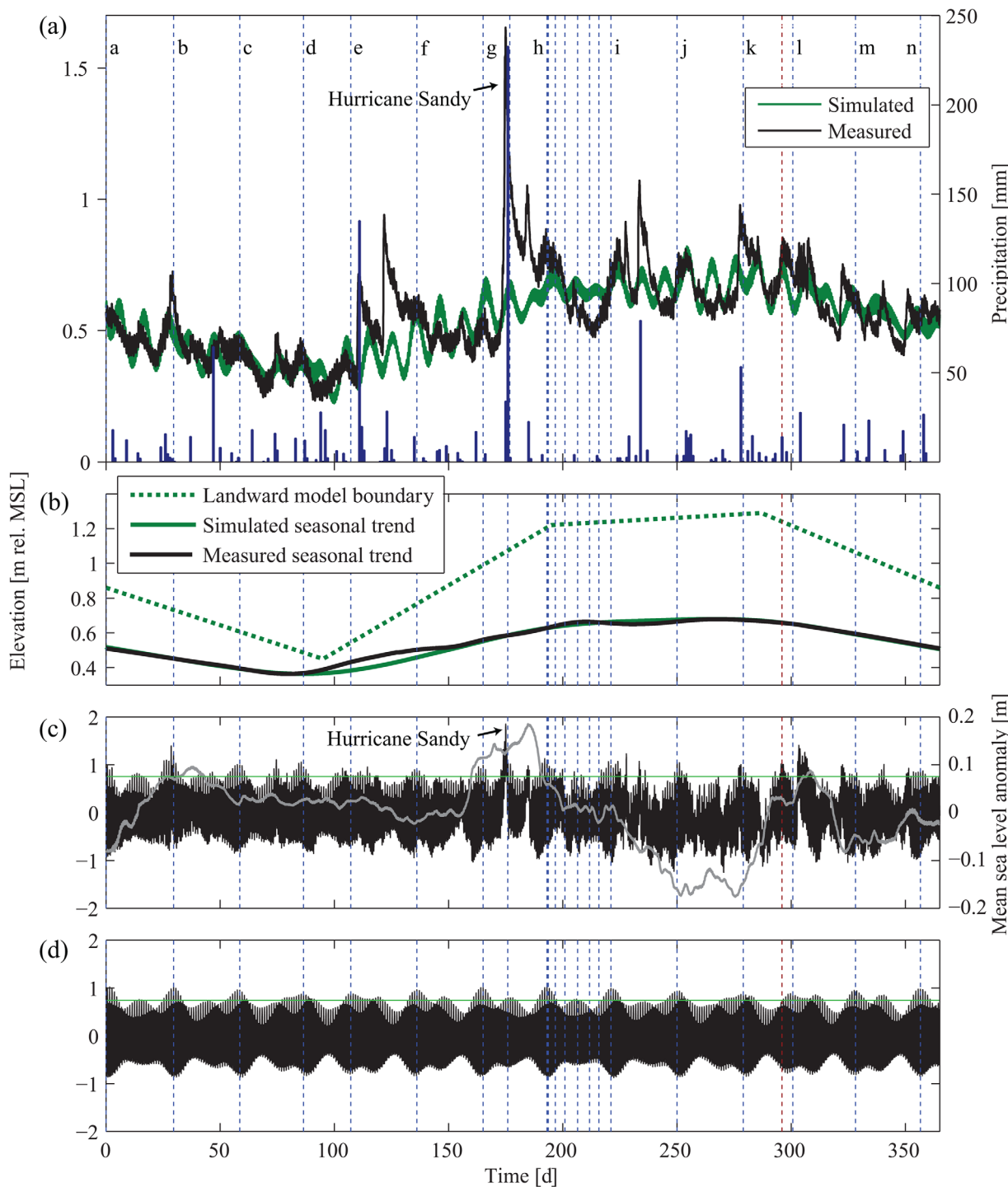


Figure 5. (a) Daily precipitation and measured and simulated hydraulic heads at the dune well; HS = Hurricane Sandy sampling event; (b) smoothed measured and simulated heads at dune well with the landward model head boundary; (c) measured tide (black) and seasonal mean sea level anomaly (gray); (d) tidal signal used in the model. Vertical blue lines denote sampling events. Vertical red line indicates timing of the tracer test. The horizontal green line on the tidal plots indicates the berm elevation. Time is days since 7 May 2012.

over monthly spring-neap cycles and up to 100 cm in response to precipitation events. On the seasonal time scale, the water table oscillated by about 30 cm.

3.1.2. Tracer Experiment

The residence time and velocity of circulating salt water were calculated by tracking the movement of the center of the tracer plume along its flow path with time. The center of the plume and discharge location

Table 1. Tidal Constituents Used in the Fitting Equation

Name	Amplitude (m)	Phase (rad)	Frequency (rad s ⁻¹)	Description
M ₂	0.616	0.543	1.41×10^{-4}	Principle lunar semidiurnal
S ₂	0.108	0.991	1.45×10^{-4}	Principle solar semidiurnal
N ₂	0.134	0.183	1.38×10^{-4}	Larger lunar elliptic semidiurnal
K ₁	0.103	3.520	7.29×10^{-5}	Lunar diurnal
O ₁	0.074	3.292	6.76×10^{-5}	Lunar diurnal

was interpreted from the bromide concentration contours mapped over the sampling ports. The maximum error in the position of the center of the plume is the distance between sampling ports: up to 80 cm vertically and 4 m horizontally, though the actual error is likely less. The results (supporting information Figure S1) showed that seawater that entered the beach aquifer at the high tide mark flowed predominantly seaward before discharging across the lower beachface. The average velocity of the plume was 1.6 m/d, and the center of the plume began to exit the aquifer 7 days after injection. This velocity is close to the 1 m/d flow rate measured in a sandy beach by *Michael et al.* [2005] and less than the 10 m/d velocity measured by *Boufadel and Bobo* [2011]. The residence time is within the range of residence times (3–14 days) observed in other intertidal field settings [e.g., *Michael et al.*, 2005; *Abarca et al.*, 2013], but slightly shorter than a 9 day residence time simulated by *Robinson et al.* [2007b], and significantly shorter than the 66 day residence time simulated by *Lenkopane et al.* [2009].

3.1.3. Spatial and Temporal Variation in Measured Salinity

The salinity measurements revealed a cell of brackish to saline pore water overlying fresh groundwater beneath the beach surface at all sampling periods. The cell extended from the high tide mark to the lower end of the beach with salinity decreasing with depth. High salinity (>25 ppt) was found to depths of up to 3 m beneath the mid-intertidal zone. A fresh groundwater discharge zone separated the circulation cell from the lower interface located at the base of the beach.

Over a semidiurnal tidal cycle, the salinity distribution remained nearly constant (Figure 6, left). The circulation cell remained centered beneath the mid-intertidal zone extending to a maximum depth of 2.5 m. This is consistent with results of numerical modeling studies [e.g., *Ataei-Ashtiani et al.*, 1999; *Mao et al.*, 2006; *Robinson et al.*, 2007a, 2007b, 2007c].

Over the monthly spring-neap cycle, the location of the circulation cell shifted and its size changed somewhat in response to changes in tidal amplitude (Figure 6, right). The cell moved downward from the backshore depression 4 days after the first spring tide, and then seaward before migrating upward near the beachface-MSL intersection following the second spring tide (206 days). Salinity below the backshore and upper beachface was elevated from days 193–200 (Figure 6, s2 and s3), corresponding to the period when high tide exceeded the elevation of the berm. This led to infiltration across the backshore and a landward shift in the location of the circulation cell. Over this time interval, shallow salinity beneath the depression decreased while deeper (>1.5 m) salinity increased. As neap tide approached and the high tide elevation declined below the berm crest, fresh groundwater flowed laterally into the upper beach and salinity beneath the depression declined rapidly from 20 to 5 ppt (Figure 6, s3 and s4). This freshening continued through the remaining spring-neap cycle (Figure 6, s5–s7). Beneath the mid to lower end of the beach, salinity increased as the cell shifted seaward during the period of lower tidal amplitude (Figure 6, s3–s5). The similarity of the salt distribution during the larger monthly spring tide measurement times (s1 and s7 in Figure 6) indicates that the observed oscillating pattern repeats over monthly spring-neap cycles. The observed shift in the position of the circulation cell was different from observations at other sites where the center of the cell remained stationary below the middle of the intertidal zone over a spring-neap cycle [e.g., *Robinson et al.*, 2007a; *Abarca et al.*, 2013].

Over the seasonal cycle, the circulation cell remained in approximately the same place, but its size changed significantly in response to the inland hydraulic gradient driving fresh groundwater flow (Figure 7). Since monthly sampling took place during spring tide, the high tide level at the times shown in Figure 7 exceeded the berm elevation. The salinity distributions in each plot thus indicate a response to berm overtopping. During a decline in the dune water table from 0 to 80 days, intertidal salinities increased (Figures 5b and 7a–7e). Once the water table reached its lowest elevation (80 days; Figure 5b), the circulation cell occupied

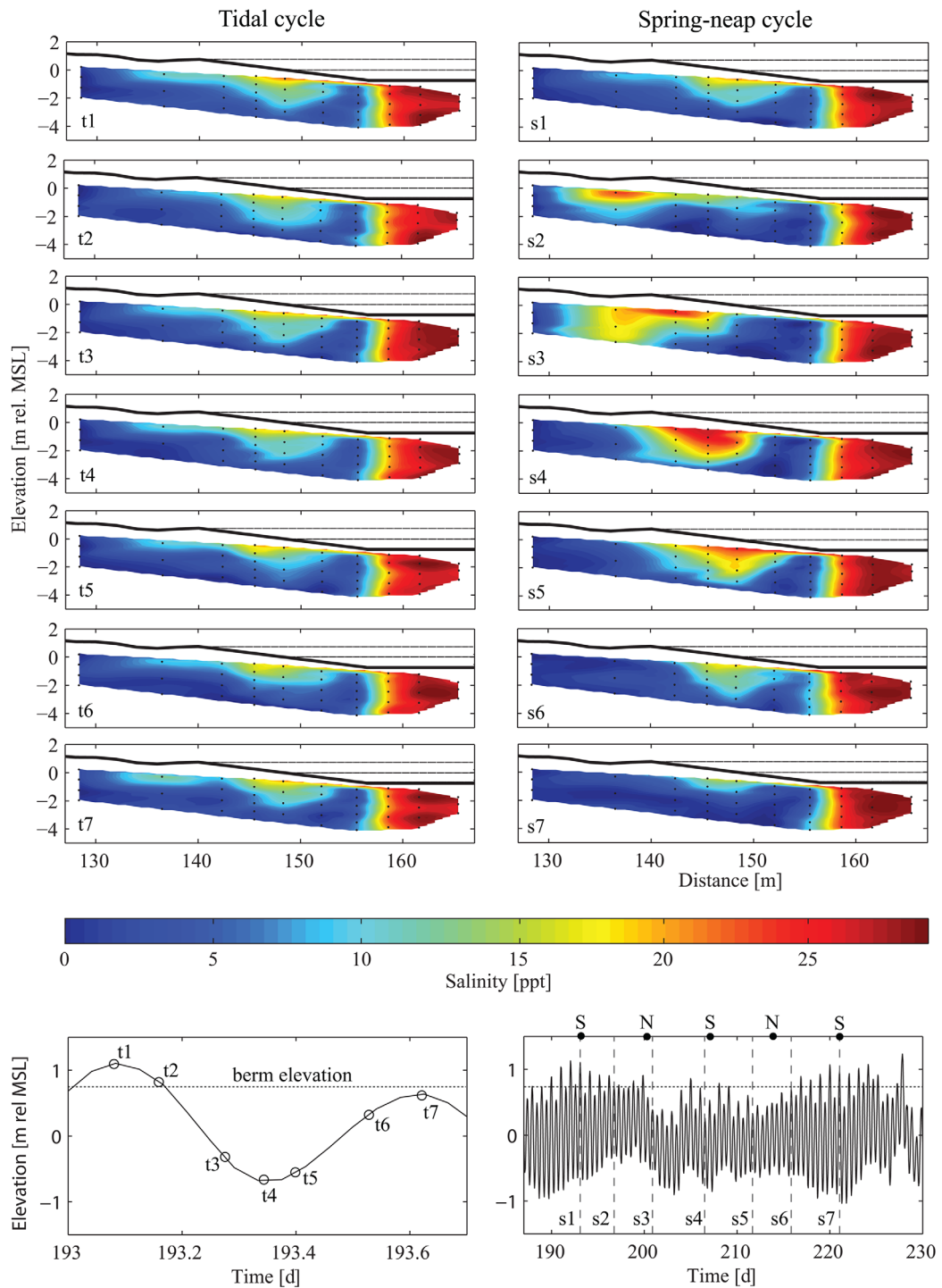


Figure 6. Measured pore water salinity over a tidal and spring-neap cycle. The horizontal line that intersects the beachface near the berm in each cross section is MHHW and the horizontal line that intersects the midbeachface is MSL. The x axis is distance relative to landward model boundary. Labels on salinity profiles correspond to sample times in the bottom two plots. The horizontal line on the tidal plots indicates the elevation of the sand surface at the berm. “S” and “N” on the spring-neap tidal plot denote spring and neap tide, respectively.

nearly the entire sampling zone (Figures 7d and 7e). As the dune water table started to rise, salinity in all parts of the aquifer below the beachface decreased until the water table reached its highest yearly elevation (268 days; Figure 5b). At this point, the beach groundwater was mostly fresh (Figures 7i and 7j). Salinity again increased when the dune water table declined for the second time (268–365 days; Figures 5b and

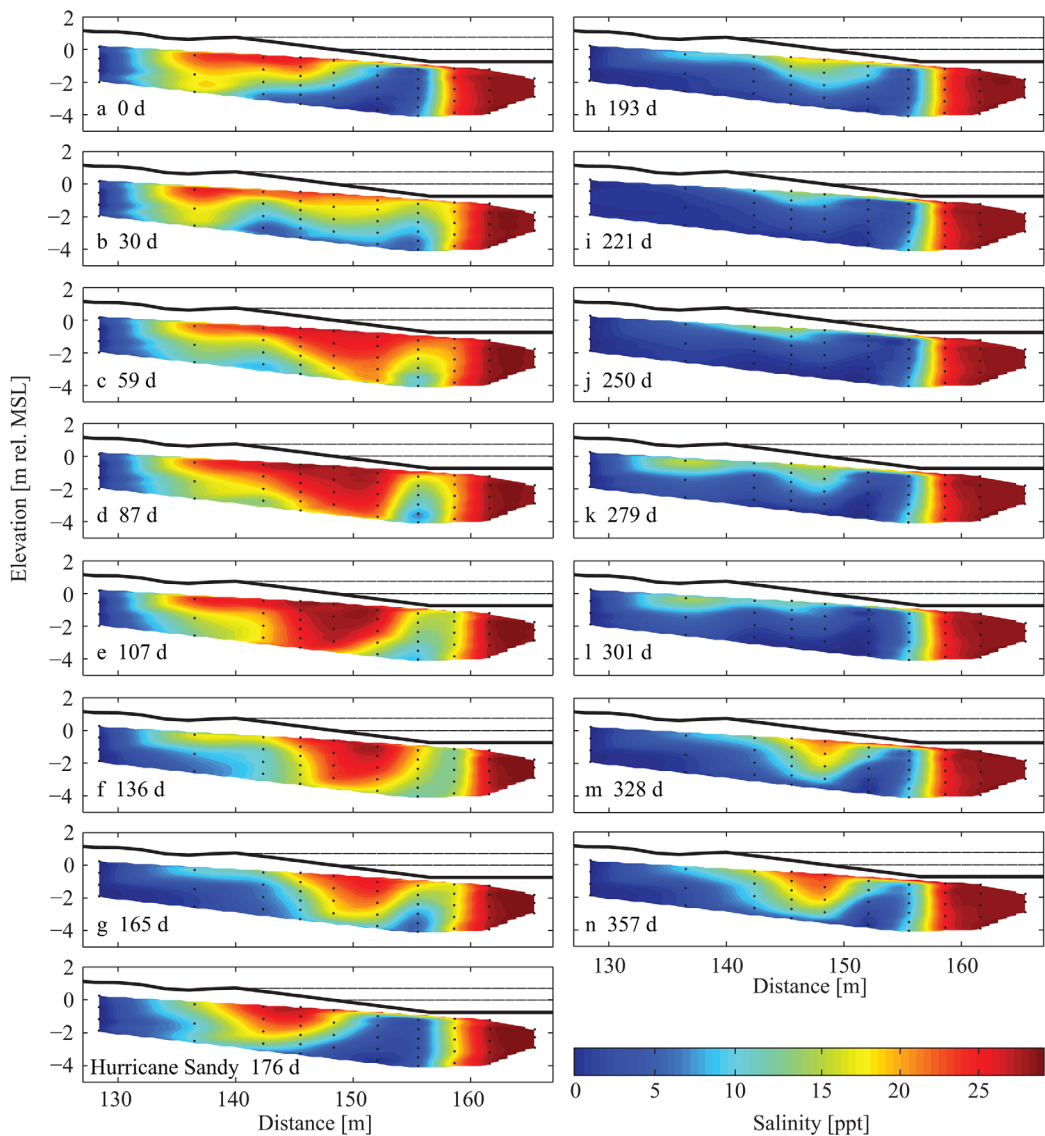


Figure 7. Measured monthly pore water salinity over a 1 year sample period. The horizontal line that intersects the beachface near the berm in each cross section is MHHW and the horizontal line that intersects the midbeachface is MSL. The x axis is distance relative to landward model boundary. Labels on cross sections correspond to sample times in Figure 5a. The location of the sampling zone is shown in Figure 4.

7k–7n). Essentially, the effectiveness of tidal forcing increased as freshwater forcing decreased. Similar results have been demonstrated in numerical modeling studies [e.g., Robinson *et al.*, 2007b; Kuan *et al.*, 2012]. Here, we extend the findings of these previous studies to include the dynamic behavior of the cell under a nonsteady landward head boundary.

Seasonal cycling of mean sea level can be an important mechanism controlling coastal aquifer salinization [e.g., Vera *et al.*, 2012; Gonnea *et al.*, 2013; Wood and Harrington, 2014]. These field studies showed that seasonally elevated mean sea levels can enhance seawater intrusion. At our site, however, seasonal variation of mean sea level did not appear to have a major influence on intertidal salinity. An approximately 15 cm positive sea level anomaly occurred between 155 and 200 days, prior to and during Hurricane Sandy (Figure 5c). During the sampling at 165 days (Figure 7g), mean sea level was elevated and the head at the dune had not yet risen due to heavy rains. However, the salinity distribution was freshened relative to the sampling at 136 days (Figure 7f), likely a response to the longer-term increase in mean head at the dune (Figure 5b). The negative mean sea level anomaly from ~225 to 285 days corresponded to the time of highest average

dune water table. The effect was an increase in the hydraulic gradient driving fresh discharge, which may have contributed to more freshening than would have occurred without the sea level anomaly. However, the simulated and measured salinities matched well (see section 3.2.1), despite the neglect of sea level anomalies in the model.

Episodic variations in rainfall, sea level, and wave action may also significantly affect the salinity distribution within the beach [e.g., Li *et al.*, 2009; Gonnea *et al.*, 2013; Robinson *et al.*, 2014]. However, our salinity measurements after Hurricane Sandy indicate that the effects of the storm were short-lived and did not substantially impact the seasonal salinity pattern (Figure 7g). The storm made landfall 85 km northeast of Cape Henlopen as a post-tropical cyclone and generated a 1.23 m storm surge at the Lewes, DE tide gauge. Just prior to the sampling at 176 days, the dune head rose more than 1 m due to heavy rains (Figure 5a), creating a strong hydraulic gradient driving fresh discharge despite the anomalous rise in mean sea level. This resulted in freshening, a landward shift in the intertidal circulation cell, and a larger zone of fresh discharge (Figure 7). However, by the next sampling event at 193 days, salinities were much lower and in line with the overall seasonal trend of decreasing salinity during that part of the year. This suggests that the beach aquifer adjusts quickly after events such as moderate storm surges and enhanced fresh groundwater inflow as a result of elevated inland hydraulic heads from rainfall.

3.2. Model Simulations

Groundwater flow and salt transport in the coastal aquifer were simulated numerically to support interpretation of field results and to further analyze dynamics in response to simultaneous forcing on multiple time scales.

3.2.1. Comparison to Field Measurements

Simulated heads, salt concentrations, and groundwater velocities and residence times are first compared to the field results to ensure consistency. The seasonal trend in simulated head at the location of the dune well matched reasonably well to measurements (Figure 5b). On an hourly time scale, deviations of up to 1.08 m occurred between measured and simulated heads (Figure 5a). This was due, at least in part, to the limitations of the numerical model, which did not account for waves, storms, or precipitation events that have been shown to affect hydraulic heads and salinity distributions in other coastal aquifers [Anderson, 2002; Smith *et al.*, 2008; Xin *et al.*, 2010; Wilson *et al.*, 2011; Robinson *et al.*, 2014]. Despite this, measured and simulated salinities at the time of the Hurricane Sandy sampling event agreed well (Figure 8). The head deviations may also have been the result of the difference between the measured tidal fluctuations (Figure 5c) and the simulated periodic boundary condition (Figure 5d). However, the measured and simulated amplitude of the head oscillations at the dune well in response to tidal forcing and spring neap variability in tidal amplitude compared favorably. The simulated head at the dune fluctuated over the same 5–10 cm range that was measured in the field. Spring-neap fluctuations were also within the 10–25 cm range of those measured at the dune. The reasonable match despite short time scale deviations indicates that the system responds to hydrologic fluctuations over longer time scales.

The model also reproduced field measurements of salinity over the spring-neap and seasonal time periods (Figure 8). Salinity variations over the semidiurnal tidal cycle also agreed favorably but are not shown in Figure 8, as there were no significant changes. In addition to matching well the salinity in the circulation cell, the model replicated variations in the positions of the fresh discharge zone and lower interface. The change in the location of the lower interface over the spring-neap cycle is evidenced by the changes in measured and simulated salinity at the shallowest port at well 8 (Figure 8). Over the seasonal time period, measured and simulated salinity at the bottom port at well 6 declined abruptly at 150 days, indicating a shift of the fresh discharge zone landward (Figure 8).

The simulated bromide tracer plume closely matched the overall migration of the experimental tracer through the subsurface (supporting information Figure S1). The simulated plume traveled predominantly seaward at an average rate of 1.4 m/d before discharging across the lower beachface 8 days after injection.

Given that the simulated heads, groundwater velocities, and salinities were satisfactorily matched to the field data, the model was used to examine: (1) the horizontal surface extent of the circulation cell; (2) the cross-sectional area of the intertidal mixing zone; and (3) fresh and total SGD across the aquifer-ocean interface over each of the three time periods.

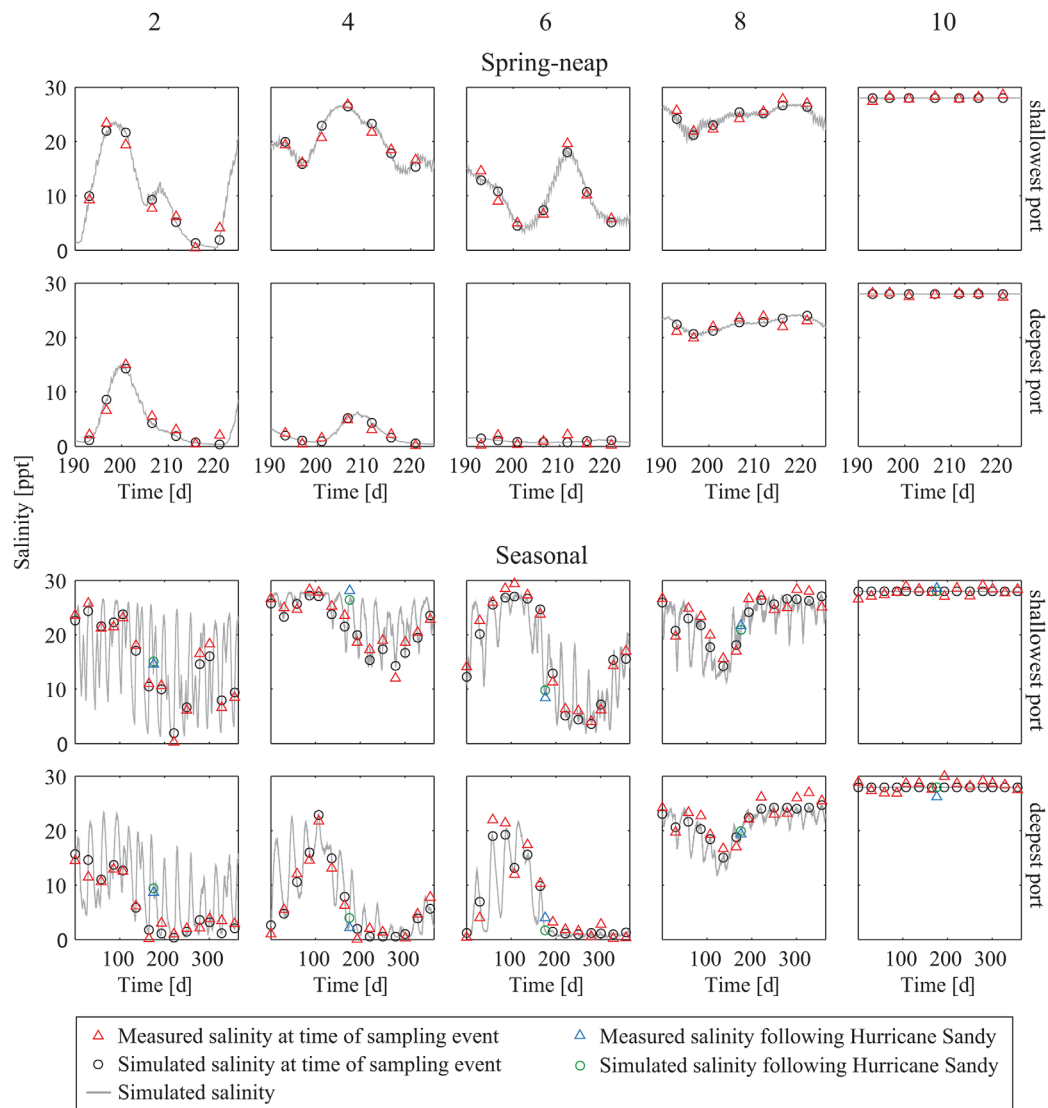


Figure 8. Observed and simulated pore water salinity for the shallowest and deepest ports for selected multilevel samplers (numbered at top) over a spring-neap and seasonal time period.

3.2.2. Tidal, Spring-Neap, and Seasonal Cycling of Shallow Salinity

Figure 9 shows salinity across the top layer of model domain over time. These near-surface salinity dynamics provide insight into the importance of each of the three time scales in controlling the horizontal surface extent of the circulation cell, fresh discharge zone, and top of the lower saltwater-freshwater interface.

The horizontal extent of the circulation cell remained largely unchanged through the semidiurnal tidal period (Figure 9a). The tidal cycle and salinity response shown in Figure 9a correspond to the same tidal cycle that was investigated in the field. Salinity across the sand surface was highest near the midsection of the intertidal zone, consistent with previous numerical modeling studies that indicate high infiltration rates from the mid-tide mark to the upper beach [e.g., Abarca *et al.*, 2013]. A region of low salinity at the berm ($x = 140$ m) separated the high salinity between the high and low water marks from a smaller region of high salinity in the backshore ($x = 134$ – 138 m; Figure 9a). The two sets of saltwater plumes, one beneath the beachface and a second below the backshore, were both simulated and observed (see a and g in Figure 6). This highlights the influence of beach morphology on the structure of the circulation cell and is consistent with findings in other modeling studies [i.e., Robinson *et al.*, 2006; Abarca *et al.*, 2013]. Salinities over other tidal cycles also were also unaffected by tidal stage.

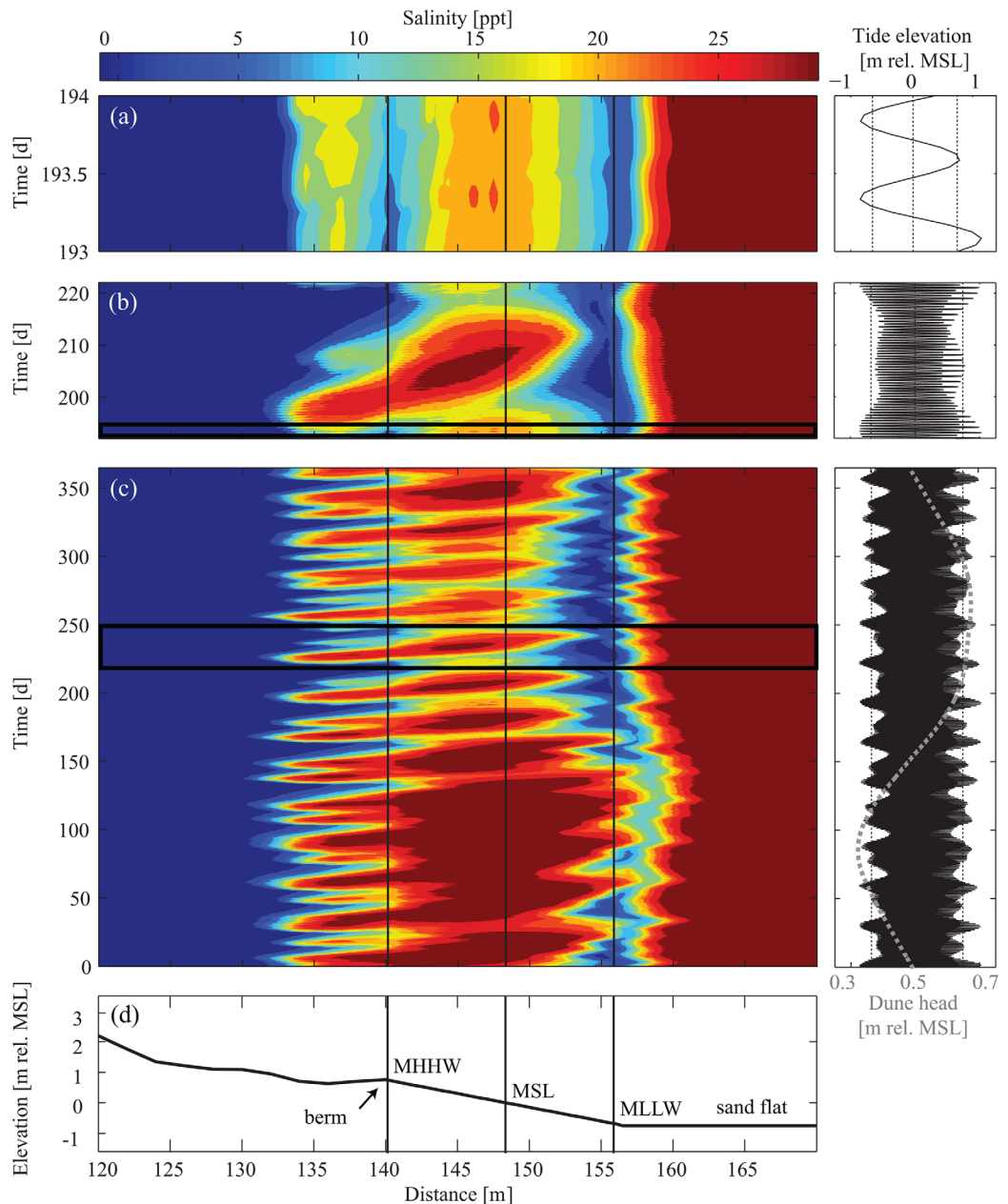


Figure 9. Simulated salinity across the top of the model domain. Salinity is shown over (a) a tidal cycle; (b) a spring-neap cycle; and (c) a seasonal cycle. (d) Beach profile. The three black vertical lines in Figures 9a–9d correspond to the location of the intersection between beachface and MHHW, MSL, and MLLW. The horizontal black rectangle in Figure 9c corresponds to the time period shown in Figure 9b. The horizontal black rectangle in Figure 9b corresponds to the time period shown in Figure 9a. The location of the berm coincides with the beachface–MHHW intersection. The dashed lines on the tide plots are MHHW, MSL, and MLLW. The x axis is distance relative to landward model boundary. Time is days since 7 May 2012.

Salinity across the top of the model and the horizontal extent of the circulation cell varied over monthly and biweekly spring-neap cycles. Figure 9b shows simulated concentrations over the same spring-neap cycle examined at Cape Shores. Salinity was generally highest across the upper beachface 4–5 days following the monthly spring tide. The salinity distribution reversed as the tidal amplitude declined; salinity beneath the upper beachface and backshore decreased while it increased across the mid-intertidal zone. The high salinity in the backshore was brought about by an increase in the landward extent of the shoreline at high tide during spring tide. This resulted in overtopping of the berm with seawater, which infiltrated in

the backshore and circulated seaward to the base of the beach over the remainder of the spring-neap cycle. The circulation of seawater from the upper to lower beach indicated a seaward shift in the location of the circulation cell. In response to the shift, the fresh discharge zone contracted by approximately 4 m (201–212 days) and the lower interface oscillated 1–2 m. Similar salinity patterns occurred over biweekly spring-neap cycles (Figure 9b). The salinity pattern and oscillation of the lower interface are consistent with field measurements (Figure 6, right), supporting the assertion that variations were due to spring-neap cycling combined with berm overtopping rather than shorter time scale events such as storms. Previous studies have also shown that the lower interface can oscillate in response to forcing by a sinusoidal tide [e.g., *Robinson et al.*, 2007b; *Xin et al.*, 2010] and over spring-neap cycles [e.g., *Abarca et al.*, 2013]. Our results indicate that these oscillations are consistent throughout the year, despite changes in the inland hydraulic gradient.

The elevation of the inland water table affected the width of the circulation cell and the location and width of the freshwater discharge zone. The width of the cell was narrowest when the water table was high, ranging from 10 to 23 m over spring neap cycles (180–300 days; Figure 9c). The cell was wider during times when the water table was low, ranging from 14 to 26 m over spring-neap cycles (50–140 days; Figure 9c). The cell expanded primarily seaward, which displaced the freshwater discharge zone and lower interface seaward. As the inland water table rose and flushing of infiltrated saltwater intensified, the horizontal extent of the cell decreased, allowing the discharge zone and lower interface to encroach landward. The inland water table had an opposite effect on the width of the discharge zone. In this case, the width of the discharge zone expanded by approximately 3 m and became fresher from 120 to 270 days as the inland water table increased. The decrease in salinity in the discharge zone can be explained by dilution from greater freshwater discharge as well as a decrease in intertidal circulation rates, which reduces dispersion along the lower interface and the amount of salt entrained in discharging groundwater [e.g., *Robinson et al.*, 2007c]. Thus, seasonal inland water table oscillations had a greater effect on the location of the freshwater discharge zone than on its width in the presence of tidal oscillations. In contrast, spring-neap cycling of tidal amplitude primarily influenced the width of the discharge zone.

3.2.3. Size of the Mixing Zone

Hydrodynamic dispersion and the transient response to forcing in the intertidal zone resulted in mixing of fresh and saline water along the perimeter of the intertidal circulation cell. This mixing zone is often biogeochemically active, so we considered its response to hydrologic fluctuations. For this purpose, we defined the size of the mixing zone as the cross-sectional area beneath the intertidal zone that fell within a range of salinity contours. Five ranges were considered; 5–95%, 10–90%, 20–80%, and 30–70% saltwater.

The mixing area varied up to 3 m^2 per tidal cycle (Figure 10a). The mixing area generally began to increase at high tide and reached a tidal cycle maximum 3–4 h later near low tide. Semidiurnal differences in tidal amplitude did not appreciably influence the size of the mixing zone.

Mixing area varied more with tidal amplitude over lunar cycles than over semidiurnal tidal cycles, as indicated by the 10 m^2 fluctuation in area that occurred over about 14 days. This is illustrated from day 193 to 207, the same time period that was investigated in the field (Figure 10b). The mixing area reached a lunar cycle maximum on day 197, 4 days after spring tide, and shrank to its smallest area on day 203.5, 5.5 days after neap tide. The 4–5.5 day time lag is likely due to infiltration across the backshore, which continued to salinize the aquifer and increase the size of the mixing zone while the high tide elevation was above the berm crest. A similar time lag time (3 days) in intertidal salinity was measured and simulated over a 2 week spring cycle by *Robinson et al.* [2007a]. The time lag and response of the mixing zone was consistent across the other spring-neap cycles.

The greatest change in the area of the mixing zone was in response to the seasonal inland water table oscillations, varying up to 115 m^3 for the 5–95% seawater contours (Figure 10). Yearly cycling in the size of the mixing zone was also greatest for the other three salinity ranges. The largest mixing zone (119 days) formed when the inland water table was near its lowest elevation (86 days). This was due to a reduction in freshwater forcing as the water table dropped, allowing the tidal circulation to strengthen and the area of the mixing zone along the boundaries of the circulation cell to increase. The opposite was the case for the smallest area, which occurred 45 days preceding the highest water table. The greater landward hydraulic gradient pushed the circulation cell up toward the surface and maintained a smaller mixing area (Figure 11). The temporal offsets between the maximum and minimum areas and the highest and lowest inland

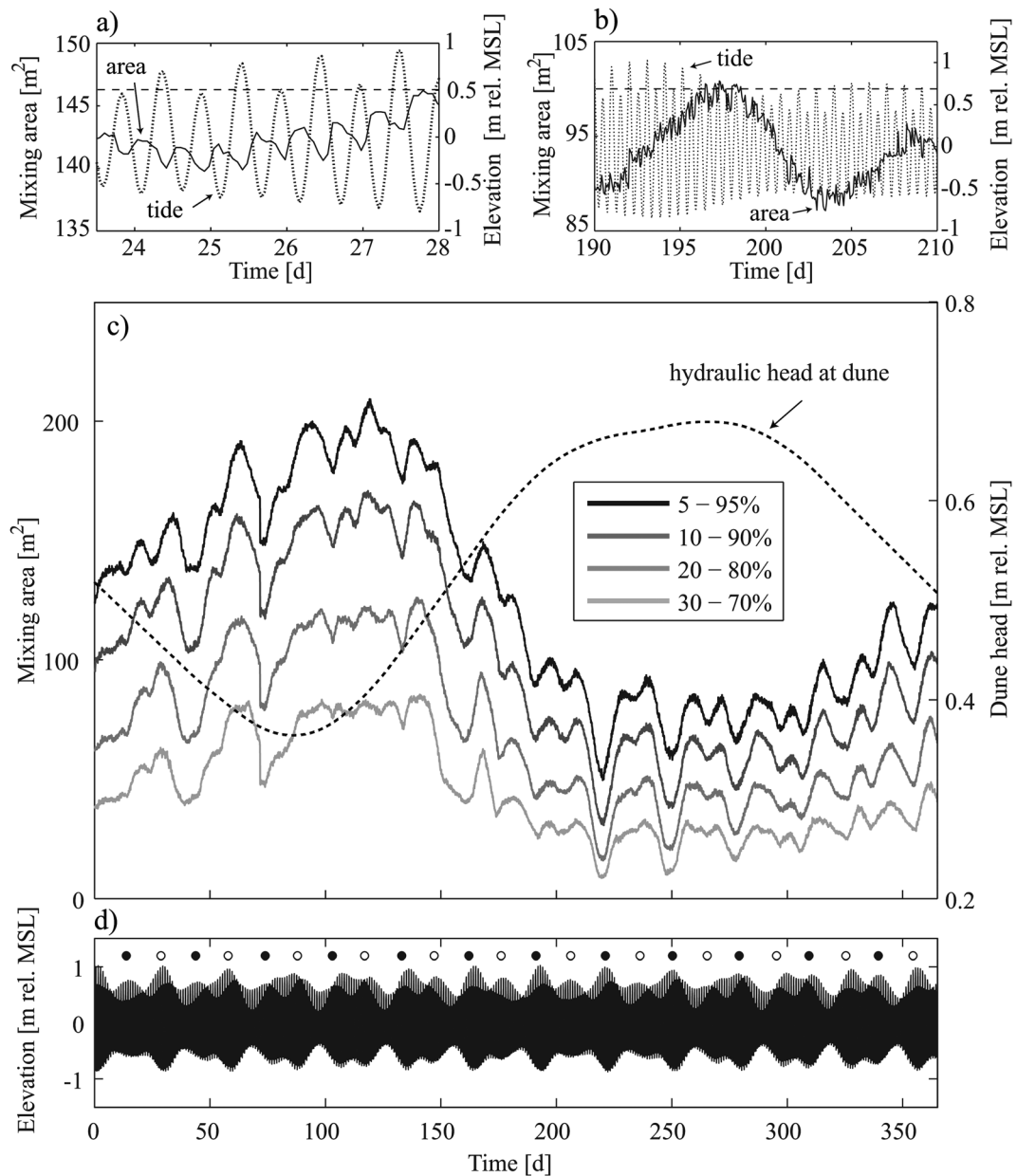


Figure 10. Simulated mixing zone area over (a) individual tidal cycles and (b) over a spring-neap cycle using the 5–95% seawater salinity contours. (c) Area of the mixing zone for different salinity ranges (as percentage of the maximum simulated salinity) over the 1 year simulation period. (d) Predicted tide used in the simulation. Symbols at the top of Figure 10d denote full (white) and new (black) moons. The horizontal dotted lines on Figures 10a and 10b indicate the elevation of the sand surface at the backshore depression.

water table elevations were caused by the effects of spring and neap tides, which were large enough to impact the timing of the largest and smallest mixing zone areas over the 1 year timeframe.

The simulation results demonstrate the importance of seasonality on mixing zone dynamics and show that shorter-term tidal and spring-neap oscillations in the size of the mixing zone are superimposed on the longer-term and more dominant seasonal cycle. These findings were qualitatively supported by the field observations, but have not been quantified prior to this work. The time lag and behavior of the mixing zone in response to the various forcing conditions was similar to that of the full circulation cell; the mixing zone expanded and contracted in-phase with the cell.

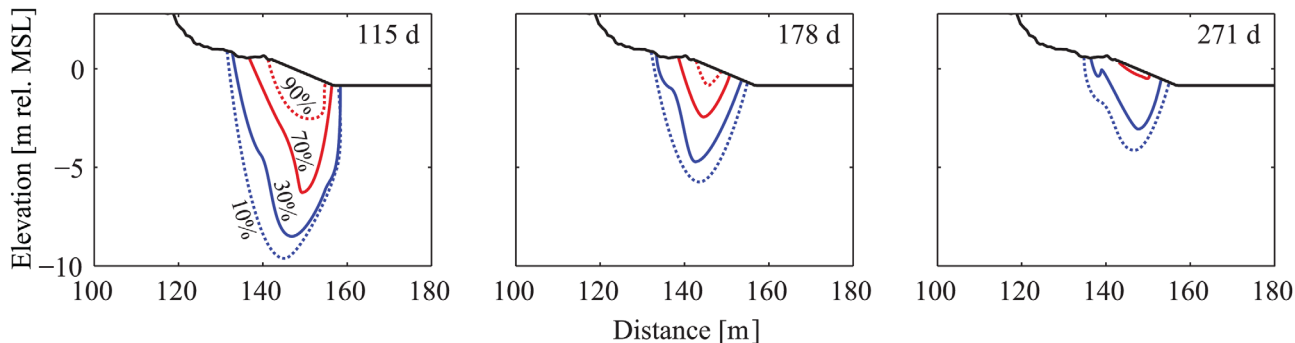


Figure 11. Simulated mixing zone area at selected times for 10–90% salt water (between the two dotted isohalines) and 30–70% salt water (between the two solid isohalines).

3.2.4. Significance of Berm Overtopping

The measured and simulated results suggest that berm overtopping and infiltration across the backshore is an important factor that regulates the formation and dynamics of the circulation cell. The observations of higher salt concentrations beneath the depression in plot s3 in Figures 6 and 9a suggest that overtopping substantially alters the spatial extent of the circulation cell. To demonstrate this importance, a simulation without a berm or backshore depression was performed with the same flow and transport boundary conditions. The slope of the beachface boundary was uniform and equal to the measured slope (1:9). In effect, the beachface was extended landward to the dune.

The beach profile affected the horizontal and vertical extent of the circulation cell considerably. Figure 12 shows the salinity distributions for simulations with and without the berm at selected times for each of the three timeframes. The results show that in the absence of berm overtopping, a secondary region of higher salt concentration beneath the upper beachface landward of 140 m (t1 and k, Figure 12) did not develop. The lack of infiltration across the upper beach profile resulted in a circulation cell that was smaller by up to 6 m horizontally and 3 m vertically compared to the simulation with the berm (Figure 12).

While the structure and extent of the circulation cell was modified by the beach profile, the general dynamics of the cell over the three time scales were preserved. In particular, phase-averaged velocity vectors over a tidal cycle indicate that the single cell of circulating seawater in the nonberm scenario was maintained when the berm was removed (Figure 12). The vectors also show that under some conditions (rows d and k, Figure 12), the backshore and intertidal salinity zones in the berm scenario connect, while under other conditions (row t1, Figure 12) these salinity zones are separate and the backshore salt water flows downward and mixes with underlying freshwater. Salinity remained largely unchanged over tidal cycles while the circulation cell expanded and contracted over monthly spring-neap cycles (rows s3–s5; Figure 12) and seasonally (rows d and k; Figure 12). Thus, similar transient behavior of the circulation cell may be expected in beaches with differing morphologies, while its structure may vary widely.

3.2.5. Fresh and Saline SGD

Both fresh and saline SGD responded to tidal stage. The top and bottom of each of the two shaded regions on a particular day in Figure 13 (top) indicate the maximum and minimum value of saline or fresh SGD that occurred over the tidal cycle on that day, respectively. For example, for the tidal cycle that occurred on day 250, fresh SGD reached a maximum of $3.0 \times 10^{-5} \text{ m}^3/\text{s}/\text{m}$ length of shoreline and a minimum of nearly zero. This large range is expected as the lower freshwater hydraulic gradient during high tide significantly reduced fresh SGD, while beach drainage and a stronger gradient during low tide promoted fresh SGD. Similarly, saline SGD decreased during high tide as the hydraulic gradient driving upward flow in the saltwater circulation cell was reduced.

Changes in tidal amplitude also impacted fresh and saline SGD (Figure 13). The ~14 and 30 day fluctuations in fresh and saline SGD correspond to spring-neap cycles. Previous field [e.g., Robinson *et al.*, 2007a] and numerical modeling [e.g., Abarca *et al.*, 2013] studies have identified similar SGD behavior.

Seasonal fluctuations affected both the average magnitude and the daily fluctuations of fresh and saline SGD. Fresh SGD varied with inland hydraulic head while saline SGD varied inversely. The percentage of total

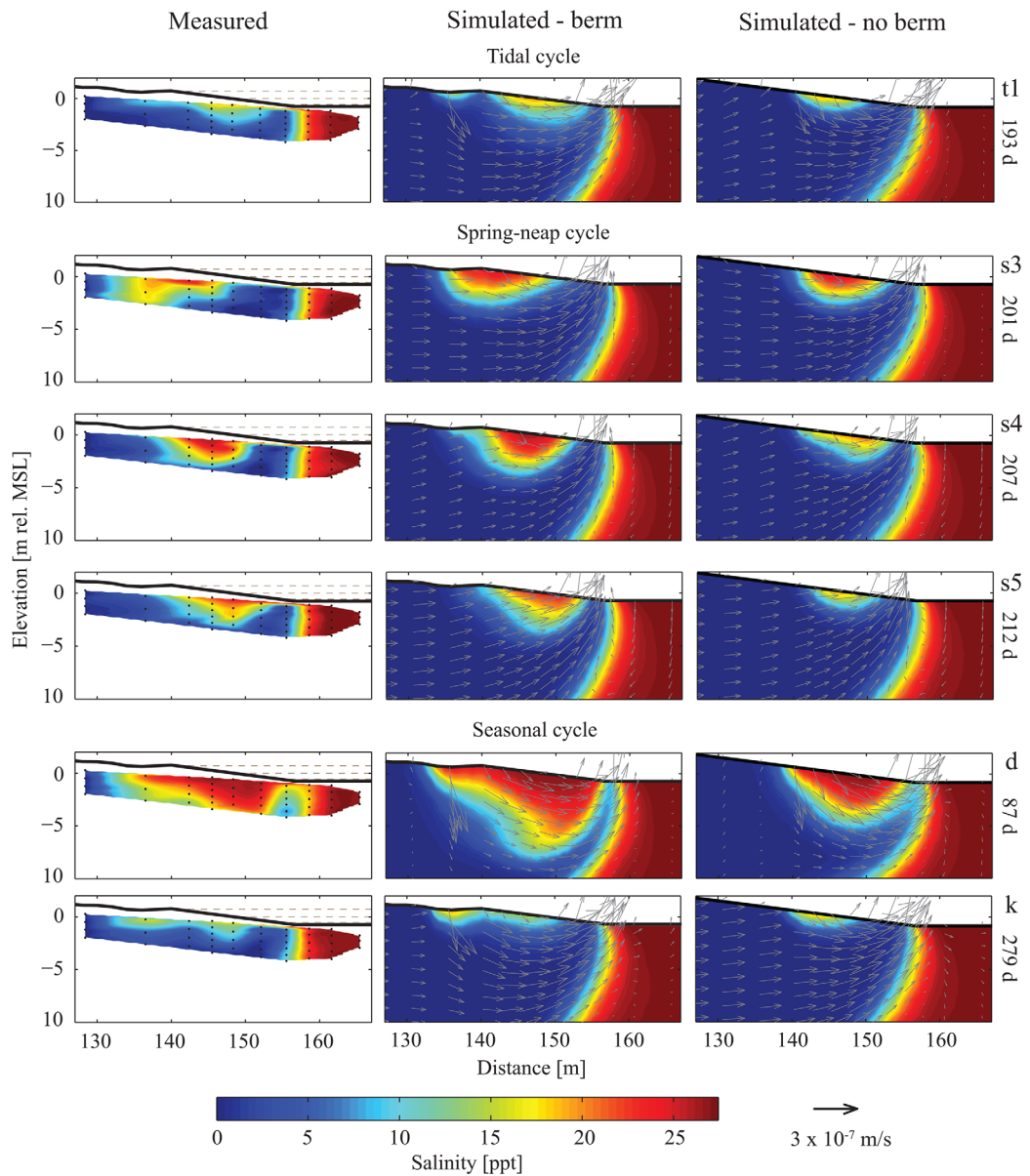


Figure 12. Measured and simulated salinity with and without a beach berm. The row labels for the tidal (t1) and spring-neap (s3–s5) cross sections correspond to those in Figure 6. The seasonal (d and k) cross sections correspond to those in Figure 5. The top, middle, and bottom horizontal dashed lines intersecting the beachface are MHHW, MSL, and MLLW, respectively. The (column 1) location of the sampling zone and (columns 2 and 3) location of the cross-sectional areas are shown in Figure 4.

SGD that was fresh therefore varied significantly, ranging from 48% to 85% over the 1 year simulation period (Figure 13, bottom). Fresh SGD increased with the inland head due to the increased freshwater hydraulic gradient. The greater inflow of fresh groundwater reduced the size of the saline circulation cell, thus reducing saline circulation and discharge, consistent with simulations [e.g., Robinson *et al.*, 2007c]. The lowest percent fresh SGD (126 days) lagged 35 days behind the lowest inland water table level. This offset was caused by the spring-neap cycling in tidal amplitude, which had a similar impact on the timing of the lowest percent of fresh SGD as it did on the timing of the minimum mixing zone area discussed in Section 3.2.2. Simulated saline SGD included the tidally driven intertidal processes investigated here, as well as offshore exchange induced by tidal pumping [e.g., Riedl *et al.*, 1972; Shum and Sundby, 1996] and density gradients [Cooper, 1959]. However, it did not include exchange driven by processes such as waves [Precht and Huettel, 2003; King *et al.*, 2009], currents [Huettel *et al.*, 1996], and bioirrigation [Cable *et al.*, 2006], which can

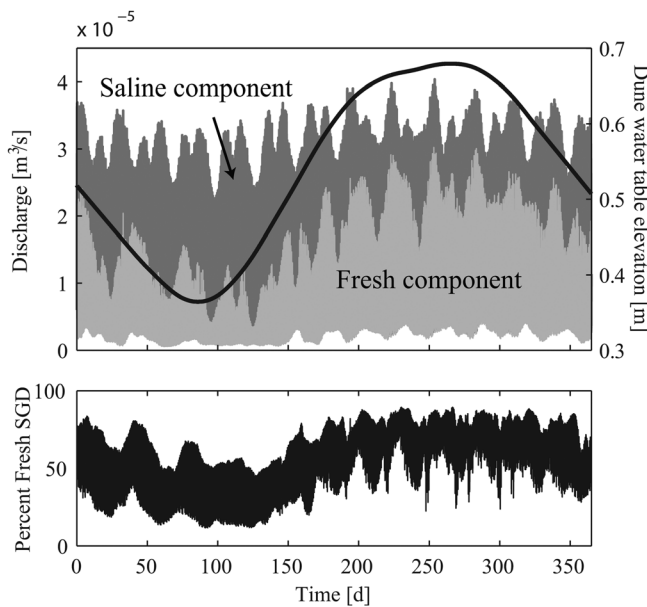


Figure 13. Stacked plot of (top) the simulated fresh and saline components of SGD with dune head and (bottom) percent of SGD that is freshwater. Discharge is per meter length of shoreline.

reactive contaminants to the coastal zone [Moore, 1999; Charette and Sholkovitz, 2002; Santos *et al.*, 2008; Spiteri *et al.*, 2008; Santoro, 2010]. The biogeochemical reactivity of these systems is ultimately linked to the physical processes of groundwater flow, mixing, and solute transport that form redox and salinity gradients and a biogeochemically active environment. The highly transient nature of these physical processes over the three time scales identified in this study is likely to impact the fate and distribution of reactive chemicals in the nearshore aquifer. For example, abiotic and biologically mediated chemical transformations occurring within the beach saltwater-freshwater mixing zone [e.g., Charette *et al.*, 2005; Beck *et al.*, 2007; Roy *et al.*, 2013] may become enhanced as the mixing zone expands during extended periods of reduced recharge and a low inland water table. In addition, variability in the biogeochemical environment may provide, within the beach aquifer, the conditions for multiple pathways of contaminant degradation, immobilization, or release. Moreover, the rate of movement of the zone of intermediate salinities along the lower saltwater-freshwater interface in response to the various forcing mechanisms may also affect the types of microbial communities in the beach aquifer. Thus, accurate predictions of the types and rates of subsurface chemical transformations and of chemical fluxes related to SGD requires a comprehensive understanding of the hydrodynamics of the beach aquifer system over a range of time scales. The results of this work may provide insight into the processes that affect biogeochemically reactive zones in beach aquifers and the time scales over which they may change.

Groundwater flow and transport processes in beach aquifers differ significantly from those occurring offshore. Residence times and flow paths tend to be shorter [e.g., Michael *et al.*, 2005; Robinson *et al.*, 2007a; Michael *et al.*, 2011; Abarca *et al.*, 2013] and oxygen levels higher [Kroeger and Charette, 2008; Charbonnier *et al.*, 2013] in the circulating seawater in the beach relative to those in circulating seawater offshore [Kroeger and Charette, 2008; Abarca *et al.*, 2013]. Because the hydrodynamics, residence times, and chemical composition of water sources differ, the mixing zone in beach aquifers is likely to exhibit different geochemical and microbial zonations than those along the lower interface and offshore. These contrasting flow and transport regimes may have important implications for the types and rates of chemical transformations that contaminants may undergo prior to discharging to nearshore marine environments.

5. Conclusions

Measurements of intertidal pore water salinity collected over three time scales were combined with a variable-density numerical model to explore the importance of tidal stage, tidal amplitude, and seasonal

induce significant seawater exchange [e.g., Santos *et al.*, 2012; Sawyer *et al.*, 2013]. Aquifer heterogeneity may also impact spatial and temporal SGD patterns [e.g., Michael *et al.*, 2003; Russoniello *et al.*, 2013; Sawyer *et al.*, 2014]. Because tidal pumping is generally small relative to intertidal circulation [Li *et al.*, 1999] and density-driven convection is relatively constant where the lower interface exists [Abarca *et al.*, 2007], the simulated variability was likely primarily due to changes in intertidal circulation.

4. Implications for Reactivity and Chemical Fluxes

Biogeochemical reactions that occur in beach aquifers can alter fluxes of nutrients, heavy metals, and other

inland water table fluctuations on the hydrodynamics and salinity distribution in a sandy beach aquifer. Measured and simulated salinities in the beach aquifer revealed an upper brackish to saline circulation cell and mixing zone with a structure, cross-sectional area, and horizontal and vertical extent that varied over tidal, spring-neap and seasonal time scales. Simulated SGD also responded to these hydrologic fluctuations.

The three time scales of forcing had different effects on the intertidal circulation cell. Observations and simulations showed that the horizontal and vertical extent of the cell was primarily controlled by seasonal changes in the inland water table, and by extension the freshwater flux. Although the circulation cell remained in approximately the same place during spring tide over a seasonal cycle, its size changed significantly. Both the circulation cell and the size of the mixing zone along its perimeter were largest during periods of low inland water table and smallest when the water table was highest. As the water table decreased, the fresh discharge zone and lower interface moved seaward due to a widening of the circulation cell that displaced the discharge zone. A high inland water table also resulted in slightly greater total SGD and a significantly higher percent of fresh SGD due to the stronger inland gradient driving fresh groundwater flow.

Changes in tidal amplitude over spring-neap cycles also influenced the intertidal dynamics, but to a lesser degree than seasonal water table fluctuations. Salinity beneath the backshore increased near spring tide as the backshore depression became inundated due to larger tidal amplitudes. The center of the circulation cell shifted seaward over the spring-neap cycle from beneath the backshore depression to the midsection of the intertidal zone. In response to this shift, the fresh discharge zone contracted and the lower interface oscillated over the fortnightly and monthly spring-neap cycles. The size of the mixing zone varied over spring-neap and tidal cycles, though to a lesser degree than over the 1 year timeframe. Tidal stage had the smallest effect on the salinity distribution and mixing zone. However, both tidal elevation and tidal amplitude significantly affected both the amount of fresh and saline SGD and their ratio.

Comparison between simulations with and without a berm and backshore depression demonstrated that berm overtopping modified the structure of the landward portion of the circulation cell. Nevertheless, the dynamic behavior of the circulation cell, fresh discharge zone, and lower interface were similar over the three time scales for both the berm and nonberm scenarios.

The results provide insight into the time scales and physical forcing mechanisms that are important to the nature of the intertidal saltwater circulation cell, the locations of fresh and saline groundwater discharge, and the position of the nearshore portion of the lower saltwater-freshwater interface. The field measurements and model results demonstrate the highly transient nature of beach groundwater, emphasize the need to consider dynamic behavior in studies of intertidal flow, transport, and chemical reactivity, and indicate that measurements taken at a single point in time should be cautiously extrapolated.

Acknowledgments

The authors thank Vincent Post for providing valuable assistance with the Periodic Boundary Condition package. The authors also thank William Ullman for insightful comments and assistance with field methods. Christopher Rusconiello, Mahfuzur Khan, and Audrey Sawyer are gratefully acknowledged for their helpful discussions and modeling insights. Suggestions and comments from Alicia Wilson, Adrian Werner, and an anonymous reviewer significantly improved this manuscript. This research was supported by National Science Foundation (NSF) grants EAR-1246554 and EAR-0910756, and Delaware EPSCoR with funds from NSF EPS-0814251 and the State of Delaware. The data used to produce the results of this paper may be obtained by contacting the corresponding author.

References

- Abarca, E., J. Carrera, X. Sánchez-Vila, and M. Dentz (2007), Anisotropic dispersive Henry problem, *Adv. Water Resour.*, 30(4), 913–926, doi: 10.1016/j.advwatres.2006.08.005.
- Abarca, E., H. Karam, H. F. Hamond, and C. F. Harvey (2013), Transient groundwater dynamics in a coastal aquifer: The effects of tides, the lunar cycle, and the beach profile, *Water Resour. Res.*, 49, 2473–2488, doi:10.1002/wrcr.20075.
- Anderson, W. P., Jr. (2002), Aquifer salinization from storm overwash, *J. Coastal Res.*, 18(3), 413–420.
- Ataie-Ashtiani, B., R. E. Volker, and D. A. Lockington (1999), Tidal effects on sea water intrusion in unconfined aquifers, *J. Hydrol.*, 216, 17–31.
- Bakhtyar, R., D. A. Barry, and A. Brovelli (2012), Numerical experiments on interactions between wave motion and variable-density coastal aquifers, *Coastal Eng.*, 60, 95–108, doi:10.1016/j.coastaleng.2011.09.001.
- Beck, A. J., Y. Tsukamoto, A. Tovar-Sanchez, M. Huerta-Diaz, H. J. Bokuniewicz, and S. A. Sañudo-Wilhelmy (2007), Importance of geochemical transformations in determining submarine groundwater discharge-derived trace metal and nutrient fluxes, *Appl. Geochem.*, 22(2), 477–490.
- Befus, K. M., M. B. Cardenas, D. V. Erler, I. R. Santos, and B. D. Eyre (2013), Heat transport dynamics at a sandy intertidal zone, *Water Resour. Res.*, 49, 3770–3786, doi:10.1002/wrcr.20325.
- Bokuniewicz, H., M. Pollock, J. Blum, and R. Wilson (2004), Submarine ground water discharge and salt penetration across the sea floor, *Ground Water*, 42(7), 983–989, doi:10.1111/j.1745-6584.2004.tb02637.x.
- Boufadel, M. C. (2000), A mechanistic study of nonlinear solute transport in a groundwater—Surface water system under steady state and transient hydraulic conditions, *Water Resour. Res.*, 36(9), 2549–2565.
- Boufadel, M. C., and A. M. Bobo (2011), Feasibility of high pressure injection of chemicals into the subsurface for the bioremediation of the exxon valdez oil, *Ground Water Monit. Rem.*, 31(1), 59–67, doi:10.1111/j1745-6584.2011.01745.
- Boufadel, M. C., Y. Xia, and H. Li (2011), Modeling solute transport and transient seepage in a laboratory beach under tidal influence, *Environ. Modell. Software*, 26(7), 899–912, doi:10.1016/j.envsoft.2011.02.005.
- Bratton, J. F., J. K. Bohlke, F. T. Manheim, and D. E. Krantz (2004), Ground water beneath coastal bays of the Delmarva Peninsula: Ages and nutrients, *Ground Water*, 42(7), 1021–1034, doi:10.1111/j.1745-6584.2004.tb02641.x.

- Cable, J. E., J. B. Martin, and J. Jaeger (2006), Exonerating Bernoulli? On evaluating the physical and biological processes affecting marine seepage meter measurements, *Limnol. Oceanogr. Methods*, 4, 172–183.
- Charbonnier, C., P. Anschutz, D. Poirier, S. Bujan, and P. Lecroart (2013), Aerobic respiration in a high-energy sandy beach, *Mar. Chem.*, 155, 10–21, doi:10.1016/j.marchem.2013.05.003.
- Charette, M. A., and E. R. Sholkovitz (2002), Oxidative precipitation of groundwater-derived ferrous iron in the subterranean estuary of a coastal bay, *Geophys. Res. Lett.*, 29(10), 1444, doi:10.1029/2001GL014512.
- Charette, M. A., and E. R. Sholkovitz (2006), Trace element cycling in a subterranean estuary: Part 2. Geochemistry of the pore water, *Geochim. Cosmochim. Acta*, 70(4), 811–826, doi:10.1016/j.gca.2005.10.019.
- Charette, M. A., E. R. Sholkovitz, and C. M. Hansel (2005), Trace element cycling in a subterranean estuary: Part 1. Geochemistry of the permeable sediments, *Geochim. Cosmochim. Acta*, 69(8), 2095–2109, doi:10.1016/j.gca.2004.10.024.
- Cooper, H. H. (1959), A hypothesis concerning the dynamic balance of fresh water and salt water in a coastal aquifer, *J. Geophys. Res.*, 64(4), 461–467, doi:10.1029/JZ064i004p00461.
- Gibbes, B., C. Robinson, L. Li, and D. Lockington (2007), Measurement of hydrodynamics and pore water chemistry in intertidal ground-water systems, *J. Coastal Res.*, 2007(50), 884–894.
- Glover, R. E. (1959), The pattern of fresh-water flow in a coastal aquifer, *J. Geophys. Res.*, 64(2), 457–459.
- Gonneea, M. E., A. E. Mulligan, and M. A. Charette (2013), Climate-driven sea level anomalies modulate coastal groundwater dynamics and discharge, *Geophys. Res. Lett.*, 40, 2701–2706, doi:10.1002/grl.50192.
- Hays, R. L., and W. J. Ullman (2007), Direct determination of total and fresh groundwater discharge and nutrient loads from a sandy beach-face at low tide (Cape Henlopen, Delaware), *Limnol. Oceanogr. Methods*, 52(1), 240–247.
- Heiss, J. W., W. J. Ullman, and H. A. Michael (2014), Swash zone moisture dynamics and unsaturated infiltration in two sandy beach aquifers, *Estuarine Coastal Shelf Sci.*, 143, 20–31, doi:10.1016/j.ecss.2014.03.015.
- Henderson, R. D., F. D. Day-Lewis, E. Abarca, C. F. Harvey, H. N. Karam, L. Liu, and J. W. Lane (2009), Marine electrical resistivity imaging of submarine groundwater discharge: Sensitivity analysis and application in Waquoit Bay, Mass., *Hydrogeol. J.*, 18(1), 173–185, doi:10.1007/s10040-009-0498-z.
- Huettel, M., W. Ziebis, and S. Forster (1996), Flow-induced uptake of particulate matter in permeable sediments, *Limnol. Oceanogr.*, 41, 309–322.
- Johannes, R. E. (1980), The ecological significance of the submarine discharge of groundwater, *Mar. Ecol. Prog. Ser.*, 3, 365–373.
- Jun, S.-C., G.-O. Bae, and K.-K. Lee (2013), Factors causing dynamic variations in the saltwater-freshwater transition zone in a beach aquifer, Mangsang, South Korea, *Hydrogeol. J.*, 21(6), 1355–1371, doi:10.1007/s10040-013-0995-y.
- King, J. N., A. J. Mehta, and R. G. Dean (2009), Generalized analytical model for benthic water flux forced by surface gravity waves, *J. Geophys. Res.*, 114, C04004, doi:10.1029/2008JC005116.
- Kohout, F. A. (1960), Cyclic flow of salt water in the Biscayne aquifer of southeastern Florida, *J. Geophys. Res.*, 65(7), 2133–2141, doi:10.1029/JZ065i007p02133.
- Kraft, J. C. (1971), The migration of Holocene sedimentary environments in coastal Delaware, *North Am. Cont. Shelf Quat.*, 14, 23–38.
- Kroeger, K. D., and M. A. Charette (2008), Nitrogen biogeochemistry of submarine groundwater discharge, *Limnol. Oceanogr. Methods*, 53(3), 1025–1039, doi:10.4319/lm.2008.53.3.1025.
- Kuan, W. K., G. Jin, P. Xin, C. Robinson, B. Gibbes, and L. Li (2012), Tidal influence on seawater intrusion in unconfined coastal aquifers, *Water Resour. Res.*, 48, W02502, doi:10.1029/2011WR010678.
- Langevin, C. D., D. T. Thorne Jr., A. M. Dausman, M. C. Sukop, and W. Guo (2008), SEAWAT version 4: A computer program for simulation of multi-species solute and heat transport, *U.S. Geol. Surv. Tech. Methods Book 6*, Chap. A22, 39 pp.
- Lebbe, L. (1999), Parameter identification in fresh-saltwater flow based on borehole resistivities and freshwater head data, *Adv. Water Resour.*, 22(8), 791–806.
- Lenkopane, M., A. D. Werner, D. A. Lockington, and L. Li (2009), Influence of variable salinity conditions in a tidal creek on riparian groundwater flow and salinity dynamics, *J. Hydrol.*, 375(3–4), 536–545, doi:10.1016/j.jhydrol.2009.07.004.
- Li, L., D. A. Barry, F. Stagnitti, and J. Y. Parlange (1999), Submarine groundwater discharge and associated chemical input to the coastal sea, *Water Resour. Res.*, 35(11), 3253–3259.
- Li, H., M. C. Boufadel, and J. Weaver (2008), Tide-induced seawater-groundwater circulation in shallow beach aquifers, *J. Hydrol.*, 352(1–2), 211–224, doi:10.1016/j.jhydrol.2008.01.013.
- Li, X., B. X. Hu, W. C. Burnett, I. R. Santos, and J. P. Chanton (2009), Submarine ground water discharge driven by tidal pumping in a heterogeneous aquifer, *Ground Water*, 47(4), 558–568, doi:10.1111/j.1745-6584.2009.00563.x.
- Mao, X., P. Enot, D. A. Barry, L. Li, A. Binley, and D.-S. Jeng (2006), Tidal influence on behaviour of a coastal aquifer adjacent to a low-relief estuary, *J. Hydrol.*, 327(1–2), 110–127, doi:10.1016/j.jhydrol.2005.11.030.
- Michael, H. A., J. S. Lubetsky, and C. F. Harvey (2003), Characterizing submarine groundwater discharge: A seepage meter study in Waquoit Bay, Mass., *Geophys. Res. Lett.*, 30(6), 1297, doi:10.1029/2002GL016000.
- Michael, H. A., A. E. Mulligan, and C. F. Harvey (2005), Seasonal oscillations in water exchange between aquifers and the coastal ocean, *Nature*, 436, 1145–1148.
- Michael, H. A., M. A. Charette, and C. F. Harvey (2011), Patterns and variability of groundwater flow and radium activity at the coast: A case study from Waquoit Bay, Mass., *Mar. Chem.*, 127(1–4), 100–114, doi:10.1016/j.marchem.2011.08.001.
- Miller, D., and W. J. Ullman (2004), Ecological consequences of ground water discharge to Delaware Bay, United States, *Ground Water*, 42(7), 959–970, doi:10.1111/j.1745-6584.2004.tb02635.x.
- Moore, W. S. (1996), Large groundwater inputs to coastal waters revealed by 226Ra enrichments, *Nature*, 380, 612–614.
- Moore, W. S. (1999), The subterranean estuary: A reaction zone of ground water and sea water, *Mar. Chem.*, 65, 111–125.
- Moore, W. S., J. L. Sarmiento, and R. M. Key (2008), Submarine groundwater discharge revealed by 228Ra distribution in the upper Atlantic Ocean, *Nat. Geosci.*, 1, 309–311.
- Post, V. E. (2011), A new package for simulating periodic boundary conditions in MODFLOW and SEAWAT, *Comput. Geosci.*, 37(11), 1843–1849, doi:10.1016/j.cageo.2011.01.012.
- Precht, E., and M. Huettel (2003), Advective pore-water exchange driven by surface gravity waves and its ecological implications, *Limnol. Oceanogr. Methods*, 48(4), 1674–1684, doi:10.4319/lm.2003.48.4.1674.
- Riedl, R. J., N. Huang, and R. Machan (1972), The subtidal pump: A mechanism of interstitial water exchange by wave action, *Mar. Biol.*, 13, 210–221.

- Robinson, C., B. Gibbes, and L. Li (2006), Driving mechanisms for groundwater flow and salt transport in a subterranean estuary, *Geophys. Res. Lett.*, 33, L03402, doi:10.1029/2005GL025247.
- Robinson, C., B. Gibbes, H. Carey, and L. Li (2007a), Salt-freshwater dynamics in a subterranean estuary over a spring-neap tidal cycle, *J. Geophys. Res.*, 112, C09007, doi:10.1029/2006JC003888.
- Robinson, C., L. Li, and D. A. Barry (2007b), Effect of tidal forcing on a subterranean estuary, *Adv. Water Resour.*, 30(4), 851–865, doi:10.1016/j.advwatres.2006.07.006.
- Robinson, C., L. Li, and H. Prommer (2007c), Tide-induced recirculation across the aquifer-ocean interface, *Water Resour. Res.*, 43, W07428, doi:10.1029/2006WR005679.
- Robinson, C., A. Brovelli, D. A. Barry, and L. Li (2009), Tidal influence on BTEX biodegradation in sandy coastal aquifers, *Adv. Water Resour.*, 32(1), 16–28, doi:10.1016/j.advwatres.2008.09.008.
- Robinson, C., P. Xin, L. Li, and D. A. Barry (2014), Groundwater flow and salt transport in a subterranean estuary driven by intensified wave conditions, *Water Resour. Res.*, 50, 165–181, doi:10.1002/2013WR013813.
- Robinson, M., D. Gallagher, and W. Reay (1998), Field observations of tidal and seasonal variations in groundwater discharge to tidal estuarine surface water, *Ground Water Monit. Rem.*, 18(1), 83–92.
- Roy, M., J. B. Martin, J. E. Cable, and C. G. Smith (2013), Variations of iron flux and organic carbon remineralization in a subterranean estuary caused by inter-annual variations in recharge, *Geochim. Cosmochim. Acta*, 103, 301–315, doi:10.1016/j.gca.2012.10.055.
- Russoniello, C. J., C. Fernandez, J. F. Bratton, J. F. Banaszak, D. E. Krantz, A. S. Andres, L. F. Konikow, and H. A. Michael (2013), Geologic effects on groundwater salinity and discharge into an estuary, *J. Hydrol.*, 498, 1–12, doi:10.1016/j.jhydrol.2013.05.049.
- Santoro, A. E. (2010), Microbial nitrogen cycling at the saltwater-freshwater interface, *Hydrogeol. J.*, 18(1), 187–202, doi:10.1007/s10040-009-0526-z.
- Santos, I. R., W. C. Burnett, J. Chanton, B. Mwashote, I. G. N. A. Suryaputra, and T. Dittmar (2008), Nutrient biogeochemistry in a Gulf of Mexico subterranean estuary and groundwater-derived fluxes to the coastal ocean, *Limnol. Oceanogr. Methods*, 53, 705–718, doi:10.4319/lo.2008.53.2.0705.
- Santos, I. R., B. D. Eyre, and M. Huettel (2012), The driving forces of porewater and groundwater flow in permeable coastal sediments: A review, *Estuarine Coastal Shelf Sci.*, 98, 1–15, doi:10.1016/j.ecss.2011.10.024.
- Sawyer, A. H., F. Shi, J. T. Kirby, and H. A. Michael (2013), Dynamic response of surface water-groundwater exchange to currents, tides, and waves in a shallow estuary, *J. Geophys. Res. Oceans*, 118, 1749–1758, doi:10.1002/jgrc.20154.
- Sawyer, A. H., O. Lazareva, K. D. Kroeger, K. Crespo, C. S. Chan, T. Stiegitz, and H. A. Michael (2014), Stratigraphic controls on fluid and solute fluxes across the sediment-water interface of an estuary, *Limnol. Oceanogr.*, 59(3), 997–1010, doi:10.4319/lo.2014.59.3.00997.
- Shum, K. T., and B. Sundby (1996), Organic matter processing in continental shelf sediments—The subtidal pump revisited, *Mar. Chem.*, 53, 81–87.
- Simmons, G. M. (1992), Importance of submarine groundwater discharge (SGWD) and seawater cycling to material flux across the sediment/water interfaces in marine environments, *Mar. Ecol. Prog. Ser.*, 84, 173–184.
- Slomp, C. P., and P. Van Cappellen (2004), Nutrient inputs to the coastal ocean through submarine groundwater discharge: Controls and potential impact, *J. Hydrol.*, 295, 64–86, doi:10.1016/j.jhydrol.2004.02.018.
- Smith, C. G., J. E. Cable, and J. B. Martin (2008), Episodic high intensity mixing events in a subterranean estuary: Effects of tropical cyclones, *Limnol. Oceanogr.*, 53(2), 666–674.
- Spiteri, C., C. P. Slomp, M. A. Charette, K. Tuncay, and C. Meile (2008), Flow and nutrient dynamics in a subterranean estuary (Waquoit Bay, MA, USA): Field data and reactive transport modeling, *Geochim. Cosmochim. Acta*, 72, 3398–3412.
- Taniguchi, M., W. C. Burnett, J. E. Cable, and J. V. Turner (2002), Investigation of submarine groundwater discharge, *Hydrol. Processes*, 16, 2115–2129.
- Turner, I. L., and R. I. Acworth (2004), Field measurements of beachface salinity structure using cross-borehole resistivity imaging, *J. Coastal Res.*, 20(3), 753–760.
- Ullman, W. J., B. Chang, D. C. Miller, and J. A. Madsen (2003), Groundwater mixing, nutrient diagenesis, and discharges across a sandy beachface, Cape Henlopen, Delaware (USA), *Estuarine Coastal Shelf Sci.*, 57, 539–552.
- Vandenbohede, A., and L. Lebbe (2005), Occurrence of salt water above fresh water in dynamic equilibrium in a coastal groundwater flow system near De Panne, Belgium, *Hydrogeol. J.*, 14(4), 462–472, doi:10.1007/s10040-005-0446-5.
- Vera, I., I. Marino-Tapia, and C. Enriquez (2012), Effects of drought and subtidal sea-level variability on salt intrusion in a coastal karst aquifer, *Mar. Freshwater Res.*, 63, 485–493.
- Vukovic, M., and A. Soro (1992), *Determination of Hydraulic Conductivity of Porous Media From Grain-Size Composition*, Water Resour. Publ., Littleton, Colo.
- Werner, A. D., and D. A. Lockington (2006), Tidal impacts on riparian salinities near estuaries, *J. Hydrol.*, 328(3–4), 511–522, doi:10.1016/j.jhydrol.2005.12.011.
- Wilson, A. M., W. S. Moore, S. B. Joye, J. L. Anderson, and C. A. Schutte (2011), Storm-driven groundwater flow in a salt marsh, *Water Resour. Res.*, 47, W02535, doi:10.1029/2010WR009496.
- Wood, C., and G. A. Harrington (2014), Influence of seasonal variations in sea level on the salinity regime of a coastal groundwater-fed wetland, *Ground Water*, doi:10.1111/gwat.12168, in press.
- Xin, P., C. Robinson, L. Li, D. A. Barry, and R. Bakhtyar (2010), Effects of wave forcing on a subterranean estuary, *Water Resour. Res.*, 46, W12505, doi:10.1029/2010WR009632.